Presynaptic Optical Modulation Enabled by Dielectric-Embedded Type-II PbS/PbSe Quantum Dots for Near-Infrared Neuromorphic Vision

Yuxiao Fang[+,1], Yuxiang Fang[+,1,2], Jiadong Shen[+,1,2], Herong Sheng[1,2], Hao Lei[3], Kang Hu[1,2], Jiaye Wu[1,2], Yueheng Sun[1,2], Hongyi Xiong[1,2], Yizhi Wang[1,2], Xinrong Li[1,2], Kanghong Wang[*,4], Jingjin Wu[*,5], Lixing Kang[*,6,7] and Chun Zhao[*,1]

1. School of Advanced Technology, Xi'an Jiaotong-Liverpool University, Suzhou 215123, China.
2. Department of Electrical Engineering and Electronics, University of Liverpool, Liverpool L69 3BX, UK.
3. Institute of Functional Nano and Soft Materials (FUNSOM), Joint International Research Laboratory of Carbon-Based Functional Materials and Devices, Soochow University, Suzhou 215123, China.
4. Department of Chemistry and Materials Science, Advanced Materials Research Center, School of Science, Xi'an Jiaotong-Liverpool University, Suzhou 215123, China
5. School of Mechanical and Electrical Engineering, Hainan University, Haikou 570228, China.
6. School of Nano-Tech and Nano-Bionics, University of Science and Technology of China, Hefei 230026, China.
7. Advanced Materials Division, Suzhou Institute of Nano-Tech and Nano-Bionics, Chinese Academy of Sciences, Suzhou 215123, China.

[+] These authors contribute equally.

* Corresponding authors: Kanghong.Wang@xjtlu.edu.cn; jingjin.wu@hainanu.edu.cn; lxkang2013@sinano.ac.cn; Chun.Zhao@xjtlu.edu.cn.

Abstract

In nighttime perception and near-infrared (NIR) neuromorphic vision, a central challenge lies in encoding weak optical inputs into stable and controllable temporal states at the sensor front end. In nocturnal mammalian retinas, AII amacrine cells achieve this function by relying on stable chemical intermediate states, presynaptic modulation, and subthreshold temporal integration. Functionally inspired by selected information-processing principles of this mechanism, we propose and demonstrate a bio-inspired device design strategy. (Reviewer 2: Q1) Through a chemical-structural co-design approach, Type-II PbS/PbSe core-shell quantum dots (QDs) are used for the first time and embedded into the dielectric layer of flexible carbon-nanotube (CNT) synaptic transistors, forming stable yet decaying photo-generated intermediate states. These states modulate the CNT channel conductance via photogating, realizing a presynaptic, non-conductive modulation. The synaptic device exhibits NIR perception covering 395-808 nm and operates with an energy consumption of 0.325 fJ per synaptic event. An 8 × 8 synaptic array enables history dependent temporal processing, generating 32 distinguishable output states under 5-bit optical inputs. Based on these properties, a reservoir computing (RC) framework is validated on a dataset exceeding 10^5 samples, achieving 94.6% accuracy in nighttime human action recognition tasks. These results establish a bio-inspired material-device-system pathway for NIR near-sensor temporal perception and computation.

Keywords: Near-infrared (NIR) neuromorphic vision, Near sensor computing, Bio-inspired synaptic modulation, Carbon nanotube (CNT) synaptic transistor.

1. Introduction

In applications such as nighttime perception, health monitoring, and intelligent surveillance, near-infrared (NIR) light has become one of the most practically valuable sensing bands due to its low susceptibility to environmental interference and high safety for human exposure. [1-11] At present, the key challenge in NIR perception is to reliably integrate limited input stimuli and convert them into stable and controllable temporal state representations, which are essential for subsequent information processing and recognition tasks. [12-19]

To address this challenge, a large number of artificial NIR vision and neuromorphic devices based on photoactive materials, including quantum dots (QDs) [2, 15, 20, 21], organic semiconductors [16, 17, 22, 23], perovskites [13, 24], and 2D semiconductors [5, 8, 12], have been developed. However, most existing research rely on direct photoelectric conversion and instantaneous current-response mechanisms. Although such mechanisms are effective for photodetection and imaging, they tend to produce transient and noise-sensitive outputs under low signal-to-noise conditions, making it difficult to establish stable intermediate states at the device level.[25-27] As a result, the capability of these devices to encode temporal information under constrained input conditions remains limited.[28, 29]

In contrast, biological scotopic vision systems process low-light inputs through fundamentally different mechanisms that do not depend on instantaneous amplitude responses.[30] For example, in the retinas of nocturnal mammals, AII amacrine cells form stable chemical intermediate states and perform continuous modulation together with subthreshold temporal integration.[31] Rather than directly transmitting signals, these cells regulate downstream neural pathways, enabling stable temporal information representations to emerge even when the input is weak and limited.[32, 33]

Inspired by this scotopic visual paradigm, we propose and demonstrate a bio-inspired device design strategy based on AII amacrine cells. Type-II PbS/PbSe core-shell QDs are used for the first time and embedded into the dielectric layer of flexible carbon-nanotube (CNT) synaptic transistors to construct stable yet decaying photo-generated intermediate states. These states continuously modulate the CNT channel conductance through photogating, enabled by the high electrostatic tunability of CNT channels,[34] leading to a presynaptic non-conductive modulation behavior. Based on this design, an 8 × 8 synaptic device array exhibits broadband 395 to 808 nm UV-NIR perception and generates 32 distinguishable fading-tail responses under 5-bit optical pulse inputs. By exploiting the multi-timescale dynamics of the array, a reservoir computing (RC) framework is constructed and achieves an action recognition accuracy of 94.6% in nighttime human motion recognition tasks. These results demonstrate the effectiveness of the proposed bio-inspired strategy for NIR temporal perception and computation at the system level.

2. Results and Discussion

2.1 Bio-Inspired Design Strategy for NIR Neuromorphic Vision

Figs. 1a-b illustrate that nocturnal mammal (e.g., cat, mouse) achieve effective motion perception under extremely low illumination by prioritizing long wavelength photon sensitivity and temporal integration rather than high spatial resolution. In the scotopic retinal pathway, rod signals are transmitted through bipolar cells and converge onto AII amacrine cells (**Fig. 1a**), which serve as a central relay for integrating and redistributing weak light inputs. As shown in **Figs. 1c-d**, AII amacrine cells operate in a continuous, non-spiking manner, where stable chemical intermediate states enable subthreshold temporal integration and inhibitory modulation of downstream pathways. This

mechanism allows weak and transient optical stimuli to be accumulated and encoded into motion related temporal information with fading memory characteristics.

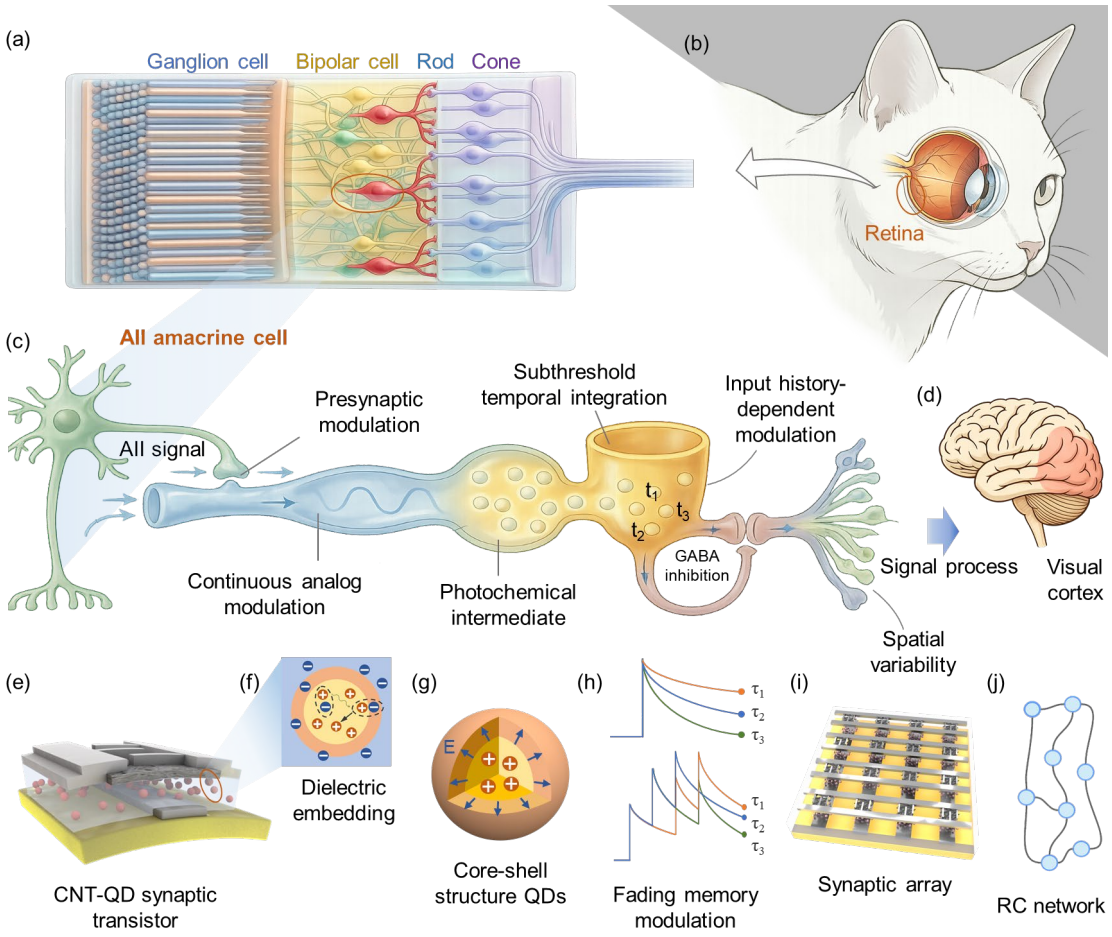

Fig. 1 Bio-inspired design and architecture of the NIR neuromorphic vision system. (a-b) Structural organization of nocturnal mammalian retina (cat). **(c-d)** Low light signal processing in AII amacrine cells, featuring presynaptic modulation and subthreshold temporal integration. Bio-inspired mapping to the artificial vision system, including **(e)** CNT-QD synaptic transistor, **(f-g)** dielectric embedded Type II PbS/PbSe QDs, **(h)** fading memory modulation, **(i)** synaptic arrays and **(j)** RC network enabled by the synaptic array.

Inspired by these scotopic processing principles, this work establishes a functional level bio inspired mapping from the retinal pathway to an artificial neuromorphic vision

system (**Figs. 1e-j**). Dielectric embedded Type II PbS/PbSe core shell QDs (**Fig. 1e**) generate stable yet decaying photo induced intermediate states via spatial electron hole separation (**Figs. 1f-g**), enabling the accumulation of weak NIR inputs without participating in charge transport. These intermediate states continuously modulate CNT channel conductance, resulting in presynaptic, non-conductive optical modulation and multi timescale EPSC tail dynamics that support subthreshold temporal integration and history dependent fading memory (**Fig. 1h**). Combined with a flexible synaptic array (**Fig. 1i**) and a RC framework (**Fig. 1j**), distinct optical and pulse histories are mapped into separable high dimensional state trajectories, reproducing at the system level the low light dynamic perception and temporal processing mediated by AII amacrine cells. This biological-to-device mapping is intended to illustrate selective functional biomimicry of weak-light temporal processing, rather than a structural or physiological reconstruction of the retinal circuit. (Reviewer 2: Q1)

2.2 Dielectric Embedded Type-II PbS/PbSe Core-Shell QDs

Motivated by the requirement for stable photoinduced intermediate states to enable subthreshold temporal integration at the device level, Type-II PbS/PbSe core-shell QDs were selected to enforce spatial separation of photogenerated electrons and holes.

Fig. 2a schematically illustrates the PbS/PbSe core-shell structure and the corresponding Type-II band alignment (CBM: PbS ≈ -4.25 eV, PbSe ≈ -4.65 eV; VBM: PbS ≈ -5.0 eV, PbSe ≈ -5.2 eV), [35] in which electrons preferentially reside in the PbSe shell while holes remain confined in the PbS core.

The transmission electron microscopy (TEM) images of the PbS/PbSe QDs with the high-resolution TEM inset revealing lattice fringes corresponding to the (200)

planes of cubic PbS with a spacing of 2.9 Å (**Supplementary Fig. S1a**). The selected-area electron diffraction (SAED) pattern in **Supplementary Fig. S1b** further confirms the cubic crystal structure with (111), (200), and (220) diffraction rings.

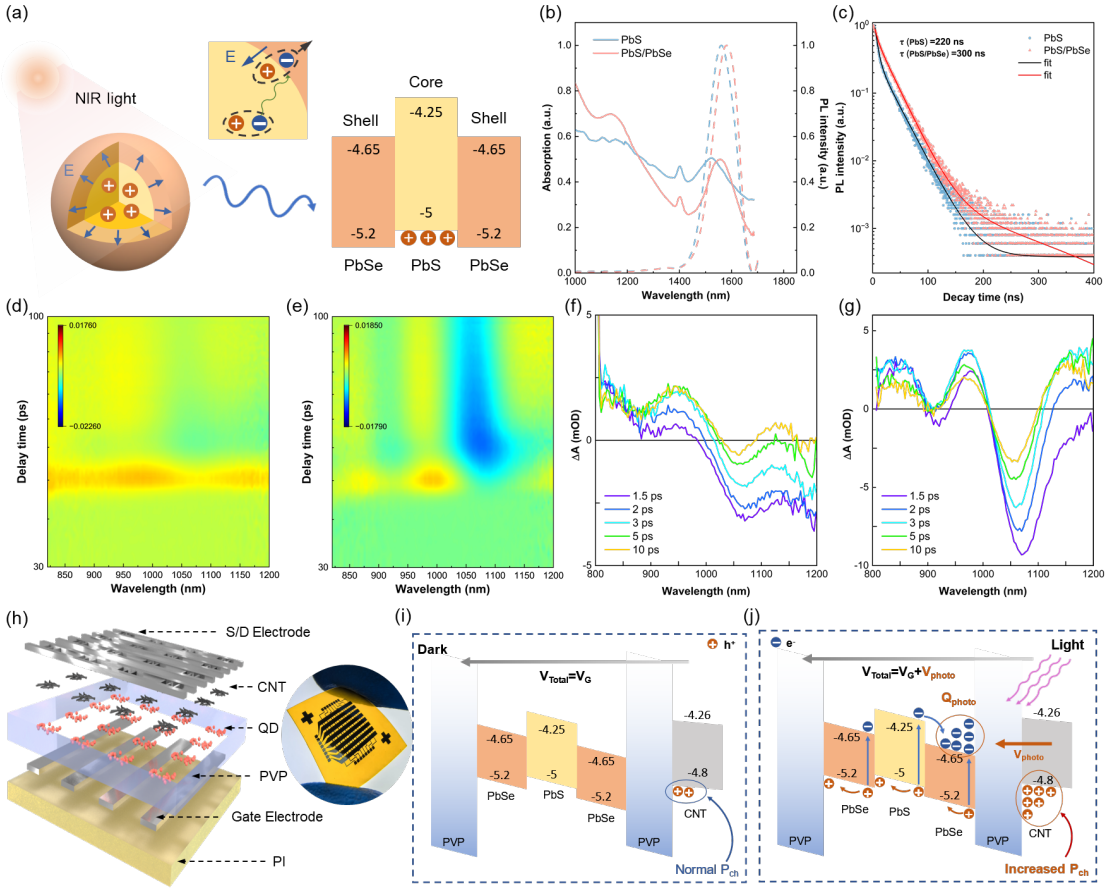

Fig. 2 Optical properties of PbS/PbSe core-shell QDs and optoelectronic mechanism of CNT-QD synaptic transistor. (a) Schematic illustration of the PbS/PbSe core-shell structure and the corresponding Type-II band alignment. **(b)** Absorption and PL spectra, **(c)** TRPL spectra and **(d-e)** TAS maps of PbS and PbS/PbSe QDs. **(f-g)** Time-resolved traces at 1070 nm probe wavelengths derived from TAS measurements. **(h)** Structural diagram and photograph of the flexible CNT-QD synaptic array. Energy-band diagrams illustrating the optoelectronic decoupling mechanism in the CNT synaptic transistor under **(i)** dark and **(j)** light environment.

High-angle annular dark-field scanning TEM (HAADF-STEM) and energy-dispersive spectroscopy (EDS) elemental mapping (**Supplementary Figs. S2a** and **S2b**) verify the well-defined core-shell configuration, where S is concentrated in the inner region and Se is distributed toward the outer shell. The successful growth of PbSe on PbS cores is supported by X-ray photoelectron spectroscopy (XPS) results of the appearance of Se 3d peak (**Supplementary Fig. S3**).

Optical characterization reveals pronounced carrier-dynamics modulation induced by shell growth. As shown in **Fig. 2b**, the absorption peak red-shifts from 1522 nm for PbS QDs to 1555 nm for PbS/PbSe QDs, accompanied by a similar red-shift in photoluminescence (PL) from 1561 to 1582 nm. Time-resolved photoluminescence (TRPL) measurements (**Fig. 2c**) show that the average carrier lifetime is prolonged from ~220 ns for PbS QDs to ~300 ns for PbS/PbSe QDs, indicating suppressed recombination enabled by the Type-II band alignment. To probe excited state dynamics, transient absorption spectroscopy (TAS) was performed using 100 fs excitation pulses at 400 nm with a broadband probe from 800 to 1200 nm. As shown in **Figs. 2d-g**, PbS QDs exhibit excited state absorption features at 945 and 1130 nm, while PbS/PbSe core shell QDs display additional excited-state absorption (ESA) peaks at 840, 970, and 1170 nm. The negative signal near 1070 nm in both samples is attributed to stimulated emission (SE). Notably, the SE decay at 1070 nm is prolonged from approximately 1.5-10 ps in PbS QDs to ~ 240 ps in PbS/PbSe QDs, consistent with the extended carrier lifetime observed in TRPL measurements (**Supplementary Fig. S4**). Specifically, as shown in **Supplementary Fig. S5**, the absorption of PbS/PbSe and PbS QDs is substantially higher than that of the CNT film across the 400-900 nm spectral region, supporting that the device photoresponse is mainly attributed to the QD layer. In addition, the stronger absorption of PbS/PbSe QDs compared with PbS QDs further

indicates the successful growth of the PbSe shell on the PbS QD surface. (Reviewer 1: Q2)

Collectively, these results demonstrate that the Type-II PbS/PbSe core-shell design enables the formation of long-lived photoinduced intermediate states through spatial carrier separation and suppressed fast recombination, providing a material-level foundation for presynaptic, non-conductive optical modulation and subthreshold temporal integration in synaptic transistor devices.

The layered device architecture is demonstrated in **Fig. 2h**, including Al gate electrode, PVP dielectric embedding PbS/PbSe QDs, CNT channel, and Ag source/drain electrode. The inset shows a photograph of the fabricated 8×8 array on the PI substrate, highlighting its flexibility and suitability for lightweight, wearable integration. **Figs. 2 i-j** demonstrate the mechanism of the photo response of the device by energy band diagram. Under pulsed illumination, photocarriers are first generated in the PbS/PbSe core-shell QDs. Owing to the Type-II band alignment, electrons preferentially transfer from the PbS core to the PbSe shell and are effectively separated from holes. [35] Due to the negative V_{GS} and large bandgap of PVP, these photogenerated electrons accumulate at the PbSe/PVP interface. Meanwhile, holes in the PbS/PbSe region are driven away from the interface by the negative gate potential. The interfacial electrons act as a quasi-floating gate and produces a photovoltage V_{photo} across the PVP dielectric. Through capacitive coupling, this photovoltage adds to the applied gate bias ($V_{Total}=V_{GS}+V_{photo}$) and induces mirror positive charges (holes) in the p-type CNT channel, thereby increasing the channel hole density P_{ch} and increasing the EPSC. In other words, the trapped electrons do not "inject" holes into CNT. They electrostatically attract holes via the gate capacitance ($\Delta Q=C_{ox}\Delta V_{photo}$). The subsequent decay of the EPSC reflects the gradual release/recombination of the interfacial electrons, consistent

with short-term synaptic plasticity.

2.3 Synaptic Transistor Arrays with Presynaptic Optical Modulation

To further verify whether the stabilized photoinduced intermediate states established at the material level (**Fig. 2**) can be effectively translated into synaptic-level temporal modulation and energy-efficient signal processing. The optoelectronic synaptic behaviors of the flexible CNT-QD transistors were systematically investigated. **Fig. 3a** shows the circuit layout of the 8×8 CNT-QD synaptic transistors array. The corresponding 64 transfer curves (I_{DS}-V_{GS}) are summarized in **Fig. 3b**. The detailed distributions of Log(I_{on}/I_{off}), threshold voltage (V_{TH}) and subthreshold swing (SS) can be found in **Supplementary Fig. S6**. The 64-device array shows controlled device-to-device variation, with coefficient of variation (CV) values of 4.0% for Log(I_{on}/I_{off}), 2.96% for V_{TH}, and 10.1% for SS. The relatively concentrated distributions of these parameters indicate controlled device-to-device variation, which supports stable biasing, consistent readout, reproducible array-level optoelectronic measurements, and scalable neuromorphic operation. (Reviewer 1: Q4) (Reviewer 2: Q5)

This uniformity highlights the reliability of the fabrication process and confirms the feasibility of scaling the devices into larger neuromorphic architectures. The I_{DS}-V_{GS} curves in **Fig. 3c** further demonstrates I_{off} increase by more than three orders of magnitude under 808 nm illumination at 10 mW cm^{-2} compared with the dark state, reaching ~1.2×10^{-8} A. A direct comparison with devices without QDs (**Supplementary Fig. S7**) further confirms the central role of dielectric-embedded Type-II PbS/PbSe core-shell QDs in the photo-synaptic response. Under representative wavelengths of 395, 450, 520, 660, and 808 nm, the QD-embedded devices show clearly enhanced EPSC amplitudes compared with the CNT-only devices, with the improvement being particularly important for extending the effective response toward the NIR region. This

result indicates that the broadband photoresponse cannot be attributed to direct CNT photoexcitation alone, but mainly arises from QD-assisted optical sensitization and photogating-mediated modulation of the CNT channel. (Reviewer 2: Q4)

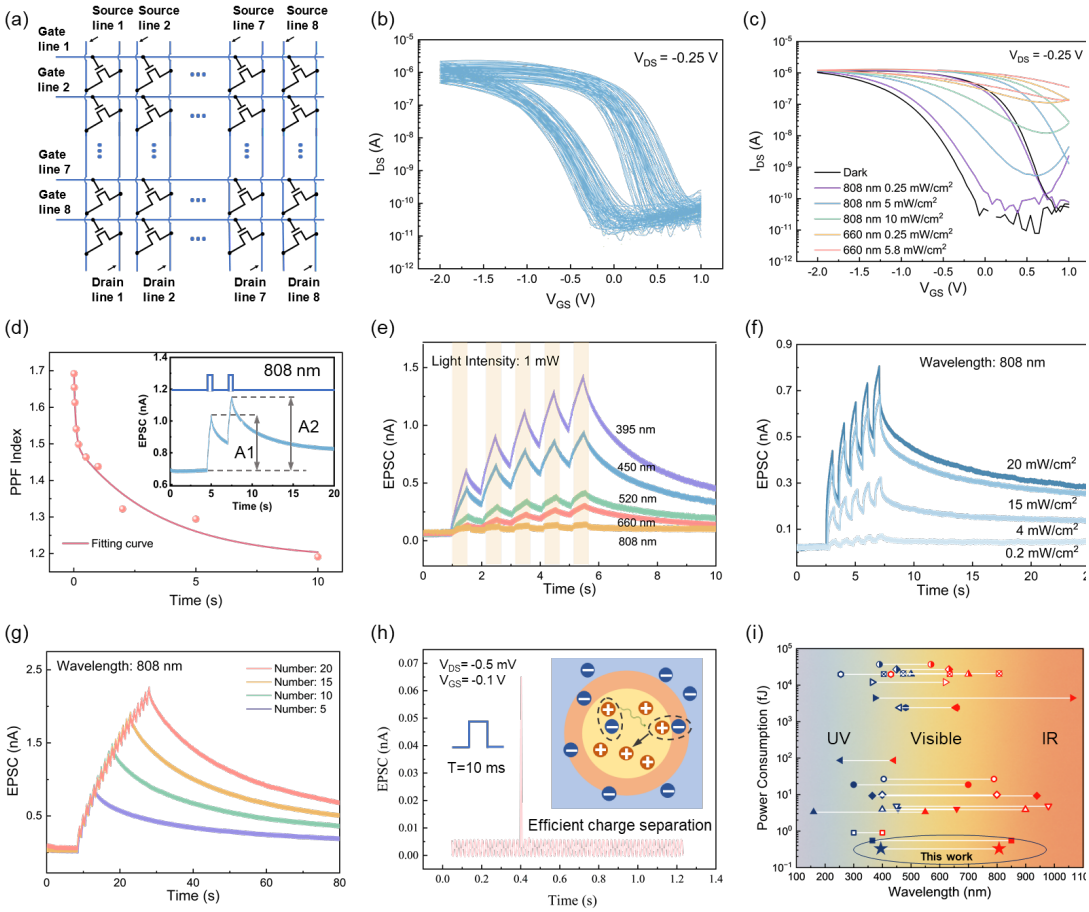

Fig. 3 Optoelectronic performance of CNT-QD synaptic arrays. (a) Circuit layout of the CNT-QD synaptic transistors array. **(b)** I_{DS}-V_{GS} curves of 64 CNT-QD synaptic transistors. **(c)** I_{DS}-V_{GS} curves under illumination with different wavelengths and powers. Synaptic photo responses including **(d)** PPF, **(e)** wavelength-dependent EPSCs, **(f)** light-intensity dependent EPSCs, **(g)** pulse-number dependent EPSCs, and **(h)** energy consumption per synaptic event. **(i)** Benchmark comparison of event energy with reported optoelectronic neuromorphic devices. **(Reviewer 1: Q5)**

Fig. 3d displays the paired-pulse facilitation (PPF) index reaches ~1.7 at a short interval of Δt = 0.01 s and gradually decays toward unity as the interval increases

beyond 10 s, reflecting the relaxation of residual photogenerated carriers. The measure PPF curves are displayed in **Supplementary Fig. S8**. **Fig. 3e** shows the broadband optical modulation capability of the CNT-QD synaptic transistors. Under 395 to 808 nm illumination, EPSC amplitudes increased from ~1 nA (808 nm) at to ~2.4 nA (395 nm) under 1 mW/cm^2 light intensity.

As shown in **Fig. 3f**, the EPSC increases continuously from ~0.08 nA (0.2 mW/cm^2) to ~0.8 nA (20 mW/cm^2) under 808 nm illumination, corresponding to nearly a 100-fold enhancement. Repeated optical pulses induce a cumulative enhancement of EPSC amplitude (**Fig. 3g**), increasing from ~0.8 nA (5 pulses) to ~2.3 nA (20 pulses) at 808 nm. Similar pulse-number-dependent strengthening behavior is observed at 660 nm (**Supplementary Fig. S9**). Moreover, increasing pulse width and pulse frequency monotonically enhances EPSC amplitudes (**Supplementary Figs. S10** and **S11**), confirming robust temporal charge accumulation and integration enabled by the stabilized photoinduced intermediate states. In addition, the retention behavior can be tuned by gate bias (**Supplementary Fig. S12**), consistent with the p-type transport characteristics of the CNT channel.

Benefiting from photogating-mediated presynaptic optical modulation enabled by dielectric-embedded Type-II PbS/PbSe QDs, the CNT-QD synaptic transistors exhibit low electrical event energy. As shown in **Fig. 3h**, according to equation (1):

$$E \approx I_{DS} \times V_{DS} \times t \quad (1)$$

Under infrared illumination at 0.2 mW cm^{-2} with V_{GS} = -0.1 V, V_{DS} = -0.5 mV, and an optical pulse duration of 10 ms, an I_{DS} of ~0.065 nA is generated, corresponding to an energy consumption of ~0.325 fJ per optically triggered synaptic event. (Reviewer 1: Q5) Performance benchmarking against previously reported optoelectronic synaptic devices (**Fig. 3i**) indicates that the devices achieve competitive energy efficiency while

maintaining broadband photosensitivity from UV to NIR. [3, 4, 13, 15, 36-52] The detailed performance information is listed in **Supplementary Table S1.** Beyond low event energy, the CNT-QD synaptic transistor also benefits from a structurally decoupled design, in which dielectric-embedded Type-II PbS/PbSe QDs serve as the optical sensitization and charge-modulation layer, while the CNT network acts as the lateral transport channel. This configuration preserves efficient channel transport while enabling stable, decaying photo-induced states for fading-memory dynamics, allowing optical histories to be converted into distinguishable temporal states for neuromorphic encoding. (Reviewer 1: Q5)

2.4 Temporal Encoding Emergent from Multi-Timescale Synaptic Dynamics

Building on the bio-inspired synaptic dynamics demonstrated in **Fig. 3**, we further explore how the controllable EPSC tail states and intrinsic fading-memory behavior of the CNT-QD synaptic devices can be exploited for temporal information processing at the system level. **Fig. 4a** illustrates the feature extraction and encoding pipeline for human skeletal dynamics. Sequential video frames are converted into temporal coordinate trajectories of skeletal joints, from which frame-to-frame displacements (ΔAct) are calculated to capture raw motion dynamics. These temporal signals are subsequently mapped into a higher-dimensional space through random Fourier features (RFF) and linear projection, followed by masking and pooling operations to generate compact temporal features compatible with reservoir processing.

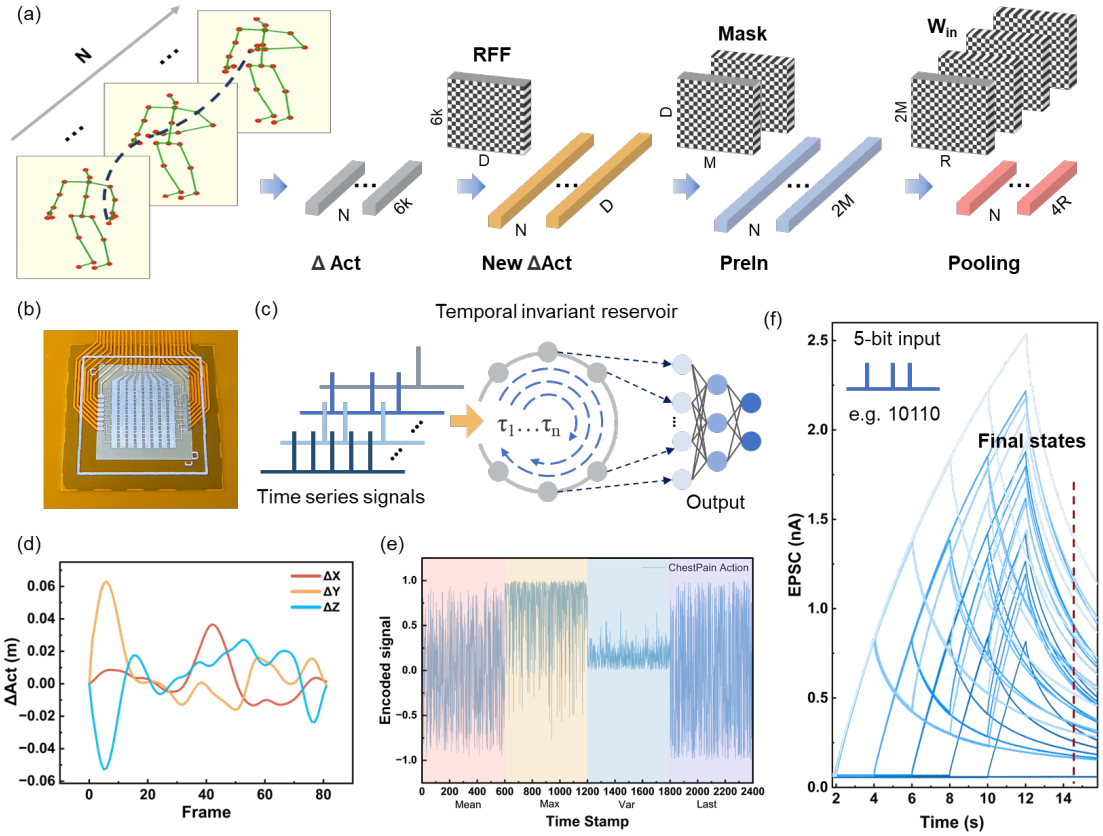

Fig. 4 Temporal encoding of human motion using synaptic dynamics. (a) Preprocessing pipeline of skeletal motion data from sequential video frame with random feature mapping, masking, and pooling. **(b)** Image of the 8 × 8 CNT-QD synaptic transistor array with external routing lines. **(c)** Temporal reservoir framework with variable τ for processing encoded time-series signals. **(d)** Motion trajectories along x, y, and z directions extracted from the dataset. **(e)** Encoded time-series signals for representative human actions (e.g., chest pain). **(f)** 5-bit pulse input and corresponding 32 EPSC final states in synaptic transistor.

Fig. 4b shows the fabricated flexible 8 × 8 CNT synaptic transistor array with fully routed interconnects, which could allow direct electrical access to each device. The array can be seamlessly interfaced with a multi-channel NI PXI measurement platform for continuous and automated testing, as demonstrated in **Supplementary Fig. S13**.

The statistical distributions of key electrical parameters have been summarized in **Supplementary Fig. S6**, confirming the uniformity and stable operation of the array. These characteristics suggest that the array is well suited for further development toward real-time neuromorphic vision demonstrations and practical large-area sensing applications.

Fig. 4c illustrates the RC architecture coupled with a multilayer perceptron (MLP) classifier. It should be noted that the present implementation represents a hardware-assisted RC framework: the CNT-QD synaptic array provides experimentally measured temporal reservoir dynamics, while the sequence preprocessing, feature projection, and MLP readout are implemented in software. (Reviewer 2: Q6) After feature encoding, the temporal sequences are injected into the reservoir, which consists of recurrently connected nodes with tunable time constants (τ). Importantly, the diversity and tunability of τ, originating from the bio-inspired synaptic tail dynamics, enable the reservoir to capture temporal dependencies across multiple time scales, ranging from short-lived fluctuations to longer-term motion patterns. The resulting reservoir states are then projected to the MLP for final classification.

Representative temporal dynamics are shown in **Figs. 4d-e** using the trajectory of the 7th skeletal node during a chest-pain-related action. The node's displacement across successive frames exhibits distinct fluctuations associated with abnormal upper-body motion. After RFF-based encoding and linear transformation, the original single-coordinate signal is expanded into multiple orthogonal feature dimensions, enhancing representational capacity while preserving both local variations and global motion trends for subsequent reservoir processing.

The suitability of the CNT-QD synaptic devices as hardware reservoir nodes is directly evidenced in **Fig. 4f.** Under 5-bit sequential optical inputs, each pulse sequence

generates a distinct transient EPSC state, reflecting the intrinsic fading-memory dynamics of the devices. By fitting the EPSC decay using equation (2), the extracted τ under each input condition is summarized in **Table S2**.

$$I(t) = I_0 + \Delta I_d e^{-(\frac{t-t_0}{\tau})^{\beta}} \quad (2)$$

Such a wide τ distribution confirms that the devices naturally support multi-timescale temporal encoding, which is a key requirement for efficient RC. The resulting rich and heterogeneous internal states facilitate nonlinear separation of input histories and enhance the expressive capacity and scalability of the hardware reservoir. In addition, for RC tasks, strict device-to-device identity is not required; instead, a balance between electrical uniformity and dynamical heterogeneity is desirable. While excessive variation in static transistor parameters may degrade operating consistency, moderate diversity in transient synaptic dynamics can enrich reservoir states and improve temporal feature representation. (Reviewer 2: Q5)Thus, the hardware contribution in this framework lies in the experimentally validated fading-memory states and multi-timescale transient responses of the CNT-QD synaptic device. (Reviewer 2: Q6)
Together, these results demonstrate that the bio-inspired synaptic tail dynamics, which is originally designed to emulate subthreshold temporal integration, can be directly leveraged to construct a physical reservoir for complex temporal tasks. This device-to-system transition establishes a direct link between CNT-QD synaptic hardware and neuromorphic vision applications.

2.5 System-Level Validation of NIR Neuromorphic Motion Recognition

To demonstrate the practical utility of the bio-inspired synaptic dynamics, we applied the flexible CNT-QD synaptic array to a RC-based human action recognition

framework. This task was selected because reliable recognition of human motions-particularly health-related actions-critically depends on temporal integration, fading memory, and multi-timescale dynamics, which directly correspond to the subthreshold temporal integration and tunable decay behaviors inherent to our devices. **Fig. 5a** shows the overall workflow of our skeleton-based action recognition framework. We apply this dual-branch Echo State Network (ESN)-MLP architecture to the large-scale NTU RGB+D 120 dataset, using its 3D skeleton streams as the primary input. From the full dataset, we construct a health-oriented subset comprising 60 classes, including daily activities, beneficial behaviors, and adverse symptom-related motions; among them, 21 classes are explicitly health-related, such as “headache”, “chest pain”, and “nausea/vomiting”. The complete data flow is demonstrated in **Supplementary Fig. S14**. As illustrated in **Supplementary Fig. S15**, the raw 3D joint coordinates extracted from continuous video frames are first normalized by subtracting a torso-center reference point of each frame, which could effectively remove global translation and subject-dependent offsets. After normalization, the skeletal data are separated into two branches: an upper-body branch containing 11 joints that emphasize detailed hand and arm motions, and a whole-body branch containing 25 joints that capture global trunk dynamics.

For each branch, frame-to-frame differences along the x/y/z coordinates are calculated to generate temporal velocity features, which form the input sequences for two independent reservoir layers, as described in **Supplementary Fig. S16**. Each reservoir produces a time-varying state sequence, which is subsequently compressed into four statistical descriptors. The four values of mean, maximum, variance and the last-state are extracted to obtain compact representations of the motion dynamics, following the procedure in **Supplementary Fig. S17**. Finally, the feature vectors from

the trunk and hand branches are concatenated and passed through a shallow MLP classifier, which performs nonlinear feature fusion and outputs the predicted action label.

As listed in **Table S3**, our dataset contains 60 actions categorized into normal, positive, and negative samples. The full 60 class training results are summarized in the confusion matrix of **Supplementary Fig. S18**. 10 Positive actions and 11 negative actions are demonstrated separately in **Supplementary Figs. S19** and **S20**, respectively. **Fig. 5b** shows the confusion matrix for these 21 health-related actions, where most categories fall along the diagonal, demonstrating strong intra-class consistency. This trend is maintained despite substantial inter-subject variation and viewpoint changes, as the majority of samples remain tightly clustered along the diagonal.

Fig. 5c reports the per-class recognition accuracy across all 60 actions. The circular chart clearly separates normal daily behaviors (blue), positive health behaviors (orange), and negative symptom-related actions (red), with most categories achieving over 85% accuracy. A small number of challenging classes show moderate performance, typically those characterized by highly similar global body motion but differing local hand trajectories. As shown in **Fig. 5d** and **Table S3**, the overall accuracy steadily increases with training and reaches 90.87% after 35 epochs, with the model exhibiting strong generalization behavior rather than overfitting. Key emergency actions such as headache and chest pain achieving accuracies of 95.7% and 98.12%, respectively, reflecting the sensitivity of the ESN-MLP pipeline to subtle upper-body posture deviations and hand-to-head interaction patterns.

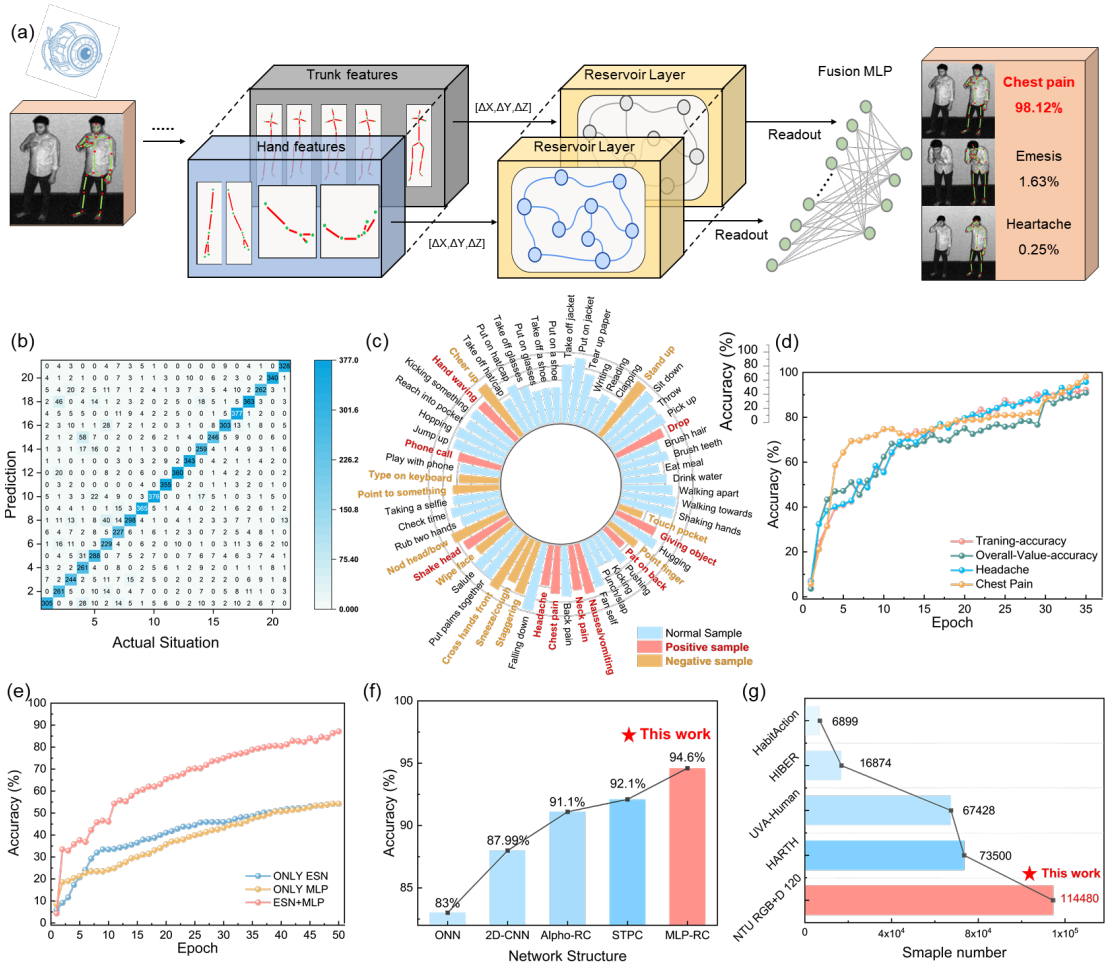

Fig. 5 Recognition performance of complex human actions under nighttime. (a) System workflow combining trunk and hand motion features with ESN and MLP for classification. **(b)** Confusion matrix across multiple actions. **(c)** Circular plot of recognition accuracy for normal (blue), positive (red), and negative (yellow) actions. **(d)** Training and testing accuracy curves over epochs. **(e)** Comparison of recognition accuracy using ESN only, MLP only, and hybrid ESN+MLP architecture. **(f)** Bar chart of action-specific recognition accuracy highlighting ten positive actions detection. **(g)** Benchmark comparison of the sample of proposed system with other reported datasets.

To further examine the contribution of each module in our framework, **Fig. 5e** compares the recognition performance of using only the ESN, only the MLP, and the combined ESN+MLP structure. The ESN alone captures temporal patterns but

converges slowly, saturating at a lower accuracy due to reliance on a linear readout. The MLP alone lacks sufficient memory for long motion sequences, as it must operate on fixed-length hand-crafted temporal features that limit its representational capacity. Their combination consistently achieves higher accuracy and faster improvement across epochs, producing a steeper learning curve by enabling the nonlinear MLP readout to exploit the rich spatiotemporal embeddings generated by the reservoir. This underscores the importance of coupling reservoir dynamics with nonlinear feature fusion.

As shown in **Fig. 5f**, although several challenging positive and negative samples exhibit moderate performance, targeted training on the 10 critical health-related actions yields an accuracy of 94.6%. Compared with network architectures reported in prior works, including ONN (83%), 2D-CNN (87.99%), Alpha-RC (91.1%), and STPC (92.1%), our method outperforms several representative action-recognition baselines on the targeted 21-class health-related actions. The actions are designed to capture early-warning nocturnal illness behaviors such as chest pain, headache, nausea/emesis, and abnormal sleep postures.[53-56] These performance gains are achieved without relying on deep or computationally heavy architectures, demonstrating the favorable balance between discriminative power and efficiency offered by the neuromorphic reservoir design. The scale of the dataset also constitutes a key distinction. As shown in **Fig. 5g**, our system is trained on over 10^5 video sequences, specifically 114,480 skeleton sequences derived from the NTU RGB+D 120-based subset. This size is one to two orders of magnitude larger than several widely used health-related behavior datasets, including HabitAction, HIBER, UVA-Human and HARTH.[57-60] This demonstrates that the proposed neuromorphic-assisted framework is capable of handling large and diverse datasets while maintaining high recognition reliability,

underscoring its potential for real-world health-monitoring and early-warning applications.

3. Conclusion

In summary, this work overcomes the long-standing bottlenecks that have hindered the practical use of Type-II PbS/PbSe QDs in neuromorphic optoelectronics. Through a chemical-structural co-design strategy, we achieved the first stable integration of Type-II QDs into flexible CNT synaptic transistors by combining defect-suppressed PbSe shell epitaxy with dielectric embedding. This approach enhances shell stability, preserves the Type-II band alignment, and electronically decouples the QDs from the CNT network, enabling efficient long-wavelength sensitization without compromising channel transport. The resulting flexible 8×8 CNT-QD synaptic array exhibits uniform device characteristics, broadband UV-NIR perception (395-808 nm), and 32 programmable fading-memory states that closely emulate biological synaptic plasticity. These NIR-driven temporal dynamics allow direct sensing and encoding of motion-related optical cues under low-light conditions. When coupled with an RC framework, the system reliably recognizes complex trunk-and-hand human actions in nighttime environments, achieving 94.6% accuracy on a $>10^5$ sequence dataset. Overall, this work demonstrates a materials-to-systems pathway that activates the long-theorized NIR sensitization capability of PbS/PbSe QDs and enables energy-efficient neuromorphic vision in low-light environments.

4. Experimental Section

4.1 Synthesis of PbS QDs and PbS/PbSe QDs

For the PbS QDs capped with oleylamine (OLA) as the ligands, $PbCl_2$ (0.8 mmol) was dissolved in OLA (2.5 mL) in a three-necked flask. OLA was used as both ligands and

solvent. The system was degassed at 100 ℃ for 30 min. Then the system was refilled with N_2 flow and the temperature was raised slowly up to 160 ℃. The solution was observed as a white suspension and the then cooled to 120 ℃. S (0.4 mmol) in OLA (0.25 mL) prepared in advance was quickly injected into the flask at the temperature and the system was kept at 100 ℃ for 120 min. Ice water was used to stop the reaction while ethanol was added to purify the QDs and PbS QDs were re-dispersed in toluene.

PbS/PbSe QDs were prepared via a successive ionic layer adsorption and reaction (SILAR) method with epitaxial growth of the PbSe shell. The PbSe shell thickness was controlled by adjusting the number of SILAR growth cycles and the amount of Pb and Se precursors supplied in each cycle, including precursor concentration and injection volume. In this work, $Pb(OA)_2$ and Se-ODE precursors were both prepared at a concentration of 0.2 M. Before PbSe shell growth, 2 mL PbS colloidal solution (~2×10^{-7} mol) and 10 mL ODE were placed in a flask. After degassing for 30 min and purging with N_2, the solution was heated to 100 °C. For each SILAR cycle, 2 mL $Pb(OA)_2$ solution was slowly injected and maintained for 10 min, followed by slow injection of 1 mL Se-ODE solution at 90 °C and another 10 min reaction. Two SILAR cycles were carried out to complete the PbSe shell growth. The flask was then cooled in a cold-water bath, and the resulting PbS/PbSe QDs were purified three times and re-dispersed in toluene. (Reviewer 2: Q2)

4.2 Device Fabrication

CNT ink was prepared by dispersing arc-discharge CNTs with poly [9-(1-octylonoyl)-9H-carbazole-2,7-diyl] (Mn = 30,000 Da) in toluene. The mixture was ultrasonicated at 0°C for 30 min to form a stable dispersion. Then the solution was centrifuged to remove the metal CNTs, insoluble impurities, and CNT bundles. The supernatant was collected as the CNT ink for subsequent device fabrication.

PVP was dissolved in propylene glycol monomethyl ether acetate (PGMEA) and stirred at 90 °C for 1 h. Poly (melamine-co-formaldehyde) (PMF) was then added as a crosslinker, together with the ionic liquid 1-ethyl-3-methylimidazolium bis (trifluoromethylsulfonyl) imide ([EMIM][TFSI]). The solution was further stirred for 10 h to ensure homogeneous blending. The chemicals were purchased from Sigma-Aldrich.

Flexible synaptic transistors were fabricated on polyimide (PI) substrates. First, Al gate electrodes (150 nm) were deposited by thermal evaporation. A PVP dielectric layer was subsequently spin-coated at 1800 rpm for 45 s and thermally annealed at 180 °C for 90 min. The surface was treated with O_2 plasma to improve wettability. CNT channels were then formed by immersing the PI/PVP substrate into the prepared CNT ink. Finally, Ag source and drain electrodes (100 nm) were deposited by thermal evaporation, completing the device structure.

4.3 Materials Characterization and Electrical/Optical Measurements

The absorption spectra were performed on an UV-Vis-NIR spectrophotometer (UV-1700 spectrometer, Shimadzu). The steady-state PL spectra were characterized by Edinburgh Instruments FLS 400. TEM images were recorded using Tecnai G2 F20. The atomic arrangement of QDs was probed by Spherical-aberration-corrected TEM (Cs-TEM, FEI Titan Themis Cubed G2 300). XPS spectra were recorded with the ARL 9800. The average lifetime of the QDs measurement was conducted in the time-correlated single-photon counting (TCSPC) mode with a laser of 455 nm. The TAS was operated with the pump pulse of 390 nm, 150 fs, 1 kHz, 6.5 J/cm^2.

The average carrier lifetime of the QDs was measured in time-correlated single-photon counting (TCSPC) mode under 455 nm laser excitation. The TRPL decay

profiles were fitted using a tri-exponential decay model, and the intensity-weighted average carrier lifetime was extracted using equation (3):

$$\tau = \frac{a_1\tau_1^2 + a_2\tau_2^2 + a_3\tau_3^2}{a_1\tau_1 + a_2\tau_2 + a_3\tau_3} \quad (3)$$

where a_i (i = 1, 2, 3) are the pre-exponential fitting coefficients of the PL decay curve and τ_i (i = 1, 2, 3) are the corresponding characteristic lifetimes. (Reviewer 2: Q3)

The electrical performance of the device was evaluated using a Keysight B1500A semiconductor parameter analyzer. The analyzer is equipped with a probe station and laser diodes with wavelength from 395 nm to 808 nm.

Supporting Information

Supporting Information is available from … or from the author.

Acknowledgments

This research was funded by National Natural Science Foundation of China (62474144, 62501489, and 62174053), Basic Research Program of Jiangsu (No. BK20250465), Centrally Guided Local Science and Technology Development Fund (2024ZYZX4025), Suzhou Industrial Park MEMS Advanced High-Performance Sensor Chip Technology Transfer Platform (CXZ2024201), Jiangsu Data Science and Cognitive Computational Engineering Research Centre, XJTLU AI University Research Centre, XJTLU Advanced Materials Research Center.

Conflict of Interest

The authors declare no competing interests

Data Availability Statement

The data that support the findings of this study are available from the corresponding author upon reasonable request

References

[1] Long, Z., Zhou, Y., Ding, Y., Qiu, X., Poddar, S., and Fan, Z., *Nat. Rev. Mater.* **2024**, 10, 128–146.

[2] Liu, J., Liu, P., Shi, T., Ke, M., Xiong, K., Liu, Y., Chen, L., Zhang, L., Liang, X., Li, H., Lu, S., Lan, X., Niu, G., Zhang, J., Fei, P., Gao, L., and Tang, J., *Nat. Commun.* **2023**, 14, 5352.

[3] Sun, X., Wang, Z., Si, C., Jiang, C., and Yang, S., *Adv. Funct. Mater.* **2024**, 35, 2411999.

[4] Zhang, J., Guo, P., Guo, Z., Li, L., Sun, T., Liu, D., Tian, L., Zu, G., Xiong, L., Zhang, J., and Huang, J., *Adv. Funct. Mater.* **2023**, 33, 2302885.

[5] Wang, F., Hu, F., Dai, M., Zhu, S., Sun, F., Duan, R., Wang, C., Han, J., Deng, W., Chen, W., Ye, M., Han, S., Qiang, B., Jin, Y., Chua, Y., Chi, N., Yu, S., Nam, D., Chae, S.H., Liu, Z., and Wang, Q., *Nat. Commun.* **2023**, 14, 1938.

[6] Xu, J., Jiang, B., Wang, W., Guo, Z., Gao, J., Hu, X., Qin, J., Ran, L., Lin, L., Cai, S., Li, Y., and Zhou, F., *Nat. Nanotechnol.* **2025**, 20, 1419–1430.

[7] Lian, H., Wang, S., Qin, Z., Dou, Z., Cheng, X., Lan, G., Li, X., Liu, A., and Dong, Q., *Device* **2025**, 3,

[8] Qu, Y., Hao, M., Hao, H., Ke, S., Li, Y., Wang, C., Xiao, Y., Jiang, B., Zhou, K., Ding, B., Chu, P.K., Yu, X.F., and Wang, J., *Adv. Mater.* **2025**, 38, e12238.

[9] Han, J., Mao, H., Lin, Y., Peng, K., Meng, L., Ding, Y., Shan, X., Tao, Y., Shi, J., Wang, Z., Zhu, H., Zhao, X., Xu, H., and Liu, Y., *Adv. Mater.* **2025**, 37, e10185.

[10] Jiang, T., Wang, Y., Zheng, Y., Wang, L., He, X., Li, L., Deng, Y., Dong, H., Tian, H., Geng, Y., Xie, L., Lei, Y., Ling, H., Ji, D., and Hu, W., *Nat. Commun.* **2023**, 14, 2281.

[11] Wang, L., Wang, H., Liu, J., Wang, Y., Shao, H., Li, W., Yi, M., Ling, H., Xie, L., and Huang, W., *Adv. Mater.* **2024**, 36, e2403538.

[12] Gao, H., Jiang, X., Ma, X., Ye, M., Yang, J., Zhang, J., Gao, Y., Li, T., Wang, H., Mei, J., Fu, X., Liu, X., Sun, T., Guo, Z., Guo, P., Chen, F., Zhang, K., Miao, J., Hu, W., and Huang, J., *Nat. Commun.* **2025**, 16, 5241.

[13] Liu, T., Yuan, Z., Wang, L., Shan, C., Zhang, Q., Chen, H., Wang, H., Wu, W., Huang, L., Chai, Y., and Meng, X., *Nat. Commun.* **2025**, 16, 4261.

[14] Huang, X., Liu, Y., Liu, G., Liu, K., Wei, X., Zhu, M., Wen, W., Zhao, Z., Guo, Y., and Liu, Y., *Adv. Funct. Mater.* **2022**, 33, 2208836.

[15] Luo, J., Tong, X., Yue, S., Wu, K., Li, X., Zhao, H., Wang, B., Li, Z., Liu, X., and Wang, Z.M., *ACS Nano* **2024**, 18, 29991–30003.

[16] Xie, C., Ke, D., Li, S., Shan, Y., Fu, C., Ren, X., Yang, L., Yang, W., and Huang, Z., *Adv. Mater.* **2026**, 38, e22683.

[17] Xu, Y., Xu, X., Huang, Y., Tian, Y., Cheng, M., Deng, J., Xie, Y., Zhang, Y., Zhang, P., Wang, X., Wang, Z., Li, M., Li, L., and Liu, M., *Adv. Mater.* **2024**, 36, e2402903.

[18] Leng, Y.B., Lv, Z., Huang, S., Xie, P., Li, H.X., Zhu, S., Sun, T., Zhou, Y., Zhai, Y., Li, Q., Ding, G., Zhou, Y., and Han, S.T., *Adv. Mater.* **2024**, 36, e2411225.

[19] Gkoupidenis, P., Zhang, Y., Kleemann, H., Ling, H., Santoro, F., Fabiano, S., Salleo, A.,

and van de Burgt, Y., *Nat. Rev. Mater.* **2023**, 9, 134–149.

[20] Zhu, Q., Li, B., Yang, D., Liu, C., Feng, S., Chen, M., Sun, Y., Tian, Y., Su, X., Wang, X., Qiu, S., Li, Q., Li, X., Zeng, H., Cheng, H., and Sun, D., *Nat. Commun.* **2021**, 12, 1798.

[21] Pan, Y., Wu, C., Bu, G., Xiang, C., Wu, R., Hu, H., Guo, T., and Li, F., *Adv. Funct. Mater.* **2025**, 35, 2505174.

[22] Liu, X., Dai, S., Jin, Y., Zhang, J., Guo, Z., Sun, T., Li, L., Guo, P., Gao, H., Liang, H., Zhang, S., Xiong, L., Zhou, Y., and Huang, J., *Nat. Commun.* **2025**, 17, 197.

[23] Wang, Y., Shan, W., Li, H., Zhong, Y., Wustoni, S., Uribe, J., Chang, T., Musteata, V.E., Castillo, T.C.H., Yue, W., Ling, H., El-Atab, N., and Inal, S., *Nat. Commun.* **2025**, 16, 1615.

[24] He, Z., Duan, H., Zeng, J., Zhou, J., Zhong, X., Wu, Z., Ni, S., Jiang, Z., Xie, G., Lee, J.-Y., Lu, Y., Zeng, Y., Zhang, B., Ying, W.B., Yang, Z., Zhang, Z., and Liu, G., *Sci. Adv.* **2025**, 11, eads2834.

[25] Shao, H., Wang, W., Zhang, Y., Gao, B., Jiang, C., Li, Y., Xie, P., Yan, Y., Shen, Y., Wu, Z., Wang, R., Ji, Y., Ling, H., Huang, W., and Ho, J.C., *Adv. Mater.* **2025**, 37, e2414261.

[26] Wang, Y., Nie, S., Liu, S., Hu, Y., Fu, J., Ming, J., Liu, J., Li, Y., He, X., Wang, L., Li, W., Yi, M., Ling, H., Xie, L., and Huang, W., *Adv. Mater.* **2024**, 36, e2404160.

[27] Zhou, G., Gu, D., Ye, J., Sun, B., Shi, H., Ran, H., Ji'e, M., Hu, X., Wang, L., Duan, S., and Ling, H., *Adv. Mater.* **2025**, 37, e08107.

[28] Ming, J., Wang, R., Fu, J., Liu, J., Wu, S., Liu, S., Shao, H., Li, Y., Wang, J., Wang, Y., Zhang, X., Xie, L., Ling, H., and Huang, W., *Nat. Commun.* **2026**, 17,

[29] Wang, Y., Shan, W., Li, H., Zhong, Y., Wustoni, S., Uribe, J., Chang, T., Musteata, V.E., Castillo, T.C.H., Yue, W., Ling, H., El-Atab, N., and Inal, S., *Nat. Commun.* **2025**, 16, 5045.

[30] Mills, S.L. and Massey, S.C., *Nature* **1995**, 377, 734–737.

[31] Voigt, T. and Wassle, H., *J. Neurosci.* **1987**, 7, 4115–4128.

[32] Nath, A., Grimes, W.N., and Diamond, J.S., *Cell Rep.* **2023**, 42, 113390.

[33] He, X., Wang, J., Fu, J., Ming, J., Wang, L., Li, W., Zheng, C., and Ling, H., *Applied Physics Letters* **2025**, 126,

[34] Zhu, M., Xiao, H., Yan, G., Sun, P., Jiang, J., Cui, Z., Zhao, J., Zhang, Z., and Peng, L.-M., *Nat. Electron.* **2020**, 3, 622–629.

[35] Du, K., Liu, G., Chen, X., and Wang, K., *J. Electrochem. Soc.* **2015**, 162, E251–E257.

[36] Dong, M., Zhang, Y., Zhu, J., Zhu, X., Zhao, J., Zhao, Q., Sun, L., Sun, Y., Yang, F., and Hu, W., *Adv. Mater.* **2024**, 36, 2409550.

[37] Guo, T., Zhang, B., Wang, X., Xiao, Y., Sun, B., Zhou, Y.N., and Wu, Y.A., *Adv. Funct. Mater.* **2023**, 33, 2303879.

[38] Talanti, S., Fu, K., Zheng, X., Shi, Y., Tan, Y., Liu, C., Liu, Y., Mu, G., Hao, Q., Weng, K., and Tang, X., *Nat. Commun.* **2025**, 16, 4311.

[39] Wang, X., Yang, S., Qin, Z., Hu, B., Bu, L., and Lu, G., *Adv. Mater.* **2023**, 35, 2303699.

[40] Wei, H., Yao, G., Ni, Y., Yang, L., Liu, J., Sun, L., Zhang, X., Yang, J., Xiao, Y., Zheng, F., and Xu, W., *Adv. Funct. Mater.* **2023**, 33, 2304000.

[41] Bai, J., He, D., Dang, B., Liu, K., Yang, Z., Wang, J., Zhang, X., Wang, Y., Tao, Y., and Yang, Y., *Adv. Mater.* **2024**, 36, 2401060.

[42] Liu, Z., Wang, Y., Zhang, Y., Sun, S., Zhang, T., Zeng, Y.J., Hu, L., Zhuge, F., Lu, B., Pan, X., and Ye, Z., *Adv. Mater.* **2025**, 37, e2410783.

[43] Huang, M., Ali, W., Yang, L., Huang, J., Yao, C., Xie, Y., Sun, R., Zhu, C., Tan, Y., Liu, X.,

Li, S., Li, Z., and Pan, A., *Adv. Sci.* **2023**, 10, 2300120.

[44] Zhu, C., Liu, H., Wang, W., Xiang, L., Jiang, J., Shuai, Q., Yang, X., Zhang, T., Zheng, B., Wang, H., Li, D., and Pan, A., *Light:Sci. Appl.* **2022**, 11, 337.

[45] Shi, X., Xu, Y., Liu, W., Jin, C., Wang, S., Sun, J., and Yang, J., *Adv. Funct. Mater.* **2024**, 34, 2401534.

[46] Serghiou, T., Fernandes, J.D., Karthikeyan, V., Assi, D.S., Vieira, D.H., Alves, N., and Kettle, J., *Adv. Funct. Mater.* **2025**, 35, 2417355.

[47] Xu, H., Hu, X., Sun, F., Sun, J., Guo, W., Liu, Y., Liu, W., Fu, X., Luo, J., and Sun, Z., *Adv. Mater.* **2025**, 37, 2504953.

[48] Xie, C., Ke, D., Li, S., Shan, Y., Fu, C., Ren, X., Yang, L., Yang, W., and Huang, Z., *Adv. Mater.* **2026**, e22683.

[49] Sun, B., Zhang, J., Meng, J., and Wang, T., *Adv. Sci.* **2026**, e24299.

[50] Zeng, Y., Hou, Z., Yu, Z., Huang, W., Lv, W., Han, Q., Zeng, T., Luo, Y., Lv, W., Fang, B., Lin, Y., Zeng, Z., and Guo, L., *Adv. Funct. Mater.* **2026**, 36, 1–12.

[51] Zhao, Z., Cao, Y., Huang, S., Fan, K., Ding, Y., Zhu, G., Li, L., Liu, Q., Deng, W., Zhao, C., and Lanza, M., *Nat. Commun.* **2026**, 17, 1–12.

[52] Zeng, J., Liu, C., Hong, Q., Zhang, B., Hong, R., Han, J., He, R., Tang, L., Zeng, P., Zhao, Z., Xie, Z., Sun, W., Zhu, W., Cao, J., Liao, L., and Zou, X., *ACS Nano* **2026**, 1–10.

[53] Cui, H., Xiao, Y., Yang, Y., Pei, M., Ke, S., Fang, X., Qiao, L., Shi, K., Long, H., Xu, W., Cai, P., Lin, P., Shi, Y., Wan, Q., and Wan, C., *Nat. Commun.* **2025**, 16, 2263.

[54] Kim, M., Jiang, X., Lauter, K., Ismayilzada, E., and Shams, S., *Nat. Commun.* **2022**, 13, 4799.

[55] Huang, Z., Shi, W., Wu, S., Wang, Y., Yang, S., and Chen, H., *Sci. Adv.* **2024**, 10, eado8516.

[56] Zhou, T., Wu, W., Zhang, J., Yu, S., and Fang, L., *Sci. Adv.* **2023**, 9, eadg4391.

[57] Li, H., Zhang, Z., and Wang, W., *arXiv preprint* **2024**,

[58] Li, Y., Wang, L., and Liu, F., *Electronics* **2022**, 11, 2526.

[59] Xie, C., Zhang, D., Wu, Z., Yu, C., Hu, Y., and Chen, Y., *IEEE T. CIRC. SYST. VID.* **2024**, 34, 490–503.

[60] Li, T., Liu, J., Zhang, W., Ni, Y., Wang, W., and Li, Z., Uav-Human: A Large Benchmark for Human Behavior Understanding with Unmanned Aerial Vehicles. *Proceedings of the IEEE/CVF Conference on Computer Vision and Pattern Recognition (CVPR)* 16266–16275 (2021).